PNAS RESEARCH ARTICLE | PHYSICS

Direct mapping of bending and torsional dynamics in individual nanostructures

Ling Tong[a,b,1], Deshuai Li[a,b,1], Ting Su[a,b], Si Gao[c], Peng Wang[c,d], Jau Tang[e], Zhong Lin Wang[a,b,f], Kebin Shi[g], and Zhi Wei Wang[a,b,h,2]

Edited by Fabrizio Carbone, Ecole Polytechnique Federale de Lausanne, Lausanne, Switzerland; received December 28, 2022; accepted May 10, 2023 by Editorial Board Member Shaul Mukamel

Investigating coherent acoustic vibrations in nanostructured materials provides fundamental insights into optomechanical responses and microscopic energy flow. Extensive measurements of vibrational dynamics have been performed for a wide variety of nanoparticles and nanoparticle assemblies. However, virtually all of them show that only the dilation modes are launched after laser excitations, and the acoustic bending and torsional motions, which are commonly observed in photoexcited chemical bonds, are absent. Unambiguous identification and refined characterization of these "missing" modes have been a long-standing issue. In this report, we investigated the acoustic vibrational dynamics of individual Au nanoprisms on free-standing graphene substrates using an ultrafast high-sensitivity dark-field imaging approach in four-dimensional transmission electron microscopy. Following optical excitations, we observed low-frequency multiple-mode oscillations and higher superposition amplitudes at nanoprism corners and edges on the subnanoparticle level. In combination with finite-element simulations, we determined that these vibrational modes correspond to out-of-plane bending and torsional motions, superimposed by an overall tilting effect of the nanoprisms. The launch and relaxation processes of these modes are highly pertinent to substrate effects and nanoparticle geometries. These findings contribute to the fundamental understanding about acoustic dynamics of individual nanostructures and their interaction with substrates.

structural dynamics | ultrafast electron microscopy | bending and torsional motions | subnanoparticle sensitivity | substrate effects

Significance

Accurately determining the vibrational dynamics in individual nanostructures is crucial for their applications, but it is also challenging. We show that, by using the self-standing graphene membrane as a support, bending and torsional modes are prominently photoexcited in triangularly shaped Au nanoprisms through ultrafast high-sensitivity dark-field imaging. This is in contrast to previous reports where photoexcited acoustic dynamics were dominated by the dilation/contraction motions. The preferential excitation of bending/torsional modes is mainly attributed to the effect of graphene substrates, which leads to the formation of internal stresses near the corners of nanoprisms. Our study also demonstrates a way to observe vibrational dynamics on light-absorptive, conductive or deformed substrates that unavoidably interact with metal nanoparticles and complicate their dynamic responses.

Spatiotemporal characterization of nanoscale acoustic responses has drawn considerable interest from both fundamental and applied research fields (1–5). Through ultrafast spectroscopy, imaging, and diffraction measurements, a general understanding of the vibrational characteristics of individual and aggregated nanoparticles has been basically reached (6–9). Subjected to ultrafast laser excitations, the fundamental and (in some cases) lower-order harmonic modes are usually launched in the nanoparticles, with vibrational frequencies that scale roughly with their dimensions (10–12). The vibrational responses of the nanoparticles can be regulated somewhat by their crystallinity, which is attributed to the effect of crystal defects on elastic moduli (13). The damping rate of photoinduced vibrations is considerably affected by their size/shape dispersion and acoustic mismatching with the surroundings (6, 14, 15). The former factor induces the issue of inhomogeneous spectral broadening, which, however, can be effectively circumvented by conducting transient dynamics investigations on individual nanostructures (16–18). Despite the observation of a rich variety of dynamics information, the nanoparticles were found to commonly dilate/contract radially or along one to several specific orientations regardless of their sizes, shapes, and crystallinity (10, 13, 17, 19, 20). In molecular compounds or polymers, bending and torsional motions of chemical bonds, in addition to stretching modes, can also be frequently launched under external excitations, with vibrational periods typically on the subpicosecond level (21, 22). However, acoustic bending and torsional modes are hardly photoexcited and were rarely observed in metal nanoparticles, whether in liquid or on supporting substrates (1, 9), and only occasionally, they appeared as a minor constituent in multiple-mode vibrations (8). A systematic investigation and mechanistic understanding of their initiation and relaxation dynamics is still lacking.

To enable quantitative measurements of the bending and torsional dynamics, an ultrafast characterization technique with high spatial resolution, ideally at the subnanoparticle level, is required. Transient absorption spectroscopy, despite its high temporal resolution, is confined to the interpretation of overall behaviors of nanoparticles or nanoparticle assembly owing to the diffraction-limited spatial resolution (10–12, 16, 17). Moreover, it lacks a detection sensitivity to the merely localized deformation occurring in these modes, which does not involve a large degree of volume variation (6). Ultrafast structural probing

Author contributions: Z.W.W. designed research; L.T., D.L., T.S., S.G., and Z.W.W. performed research; L.T., D.L., T.S., S.G., P.W., J.T., Z.L.W., K.S., and Z.W.W. analyzed data; and L.T. and Z.W.W. wrote the paper.

The authors declare no competing interest.

This article is a PNAS Direct Submission. F.C. is a guest editor invited by the Editorial Board.

[1]L.T. and D.L. contributed equally to this work.

[2]To whom correspondence may be addressed. Email: wangzhiwei@ucas.ac.cn.

This article contains supporting information online at https://www.pnas.org/lookup/suppl/doi:10.1073/pnas.2221956120/-/DCSupplemental.

Published June 12, 2023.

techniques would thus be more advantageous to the dynamics investigations. The use of ultrashort X-ray pulses, by means of Bragg coherent diffraction imaging, demonstrated the capability of revealing intraparticle lattice dynamics in individual Au nanocrystals with a diameter of several hundred nanometers (7). Further smaller particles (<100 nm) can, in principle, be investigated using ultrafast transmission electron microscopy (UTEM or 4D-TEM) at the stroboscopic mode, which combines the high spatial resolution of electron imaging with the high temporal resolution of ultrafast optical pulses (23–25). However, because of the effects of Coulomb repulsion interactions (which restrict the number of electrons available in probing pulses), and inelastic and dynamical electron diffractions, the extraction of intrananoparticle dynamics information is very challenging through standard diffraction-contrast UTEM techniques (24, 26). This issue was well addressed by the use of an ultrafast high-sensitivity-centered dark-field (UHS-CDF) imaging approach recently developed in 4D-TEM, which enables the determination of oscillation evolution in individual nanoparticles on Si_3N_4 substrates with resolution down to 3 nm (27). Nonetheless, it remains to be explored whether reliable dynamics information can be gained from metal nanoparticles on photo-absorptive and conductive substrates that may induce considerably complicated photo-responses.

In this study, we conducted systematic acoustic vibrational observations of triangular-shaped Au nanoprisms on free-standing graphene through UHS-CDF imaging. The systematic investigations led to the discovery of multiple-mode oscillations with frequencies markedly lower than those of fundamental dilation modes. We identified that these low-frequency modes are dominated by bending, torsional, and overall tilting motions, the major feature of which was replicated in finite-element simulations. The initiation of these modes is primarily induced by the contact stress preexisting at/near the Au nanoprism–graphene interface, and their temporal evolution is related to the specific morphologies of nanoparticles. These findings should be of help to the understanding of complicated acoustic dynamics phenomena in nanomaterials, especially for those metal nanoparticles/2D film composites which have received growing attention due to their unique properties and promising applications in surface-enhanced Raman scattering, biosensors, and catalytic reactions, etc. (28–30).

The synthetic Au nanoprisms generally exhibit corner-truncated triangular shapes with one of large {111} facets in contact with the substrates (*Materials and Methods*). For UHS-CDF imaging, the nanoparticles are tilted to two-beam approximation conditions, followed by the introduction of femtosecond laser pulses (~ 210 fs pulse width and ~518 nm wavelength) to initiate the dynamics of the sample (*SI Appendix*, Fig. S1). Au {220} diffraction spots are selected for recording UHS-CDF images under the condition of mild electron beam convergence. Analyses of the temporal evolution of image intensities and nanoprism dimensions allow for the extraction of transient structural dynamics information, as with the standard bright-field (BF) or dark-field (DF) UTEM imaging approaches (8, 9, 24).

Fig. 1 shows typical structural dynamics of graphene-supported Au nanoprisms with equilateral triangular shape following laser excitation. The temporally varying I/I_0 (i.e., the pumped to nonpumped intensity ratio) in Fig. 1*B* is measured from the rectangular region M indicated in Fig. 1*A*. It is evident that the structural response of the nanoprism does not feature a simple damped harmonic oscillation. This is confirmed by the FFT analysis in Fig. 1*C*, which displays the presence of four frequency peaks, 4.4, 7.4, 10.5, and 12.4 GHz. By spatially analyzing the intensity evolution across the nanoprism, nonuniform vibrational characteristics within the nanoparticle are revealed. As shown in Fig. 1*D*, the ΔI–t trace (ΔI: intensity difference with respect to nonpumped time points) measured from the square region P1 (near the nanoprism center, as marked in Fig. 1*A*) has a smaller oscillation magnitude than that from P2 (corner region). This is more evident in the intensity SD (ISD) mapping analysis (Fig. 1 *D*, *Inset*) performed over the entire relaxation duration, in which a darker core is clearly visible. The slightly smaller ISD appearing at the top left corner is related to the effect of local crystallographic orientation (*SI Appendix*, *Notes* and Fig. S2). The UHS-CDF imaging was also performed using the other {220} diffractions (*SI Appendix*, Fig. S3), which exhibit similar oscillation behaviors (smaller amplitudes at the center). Note that the application of the UHS-CDF imaging approach is crucial for the accurate mapping of intrananoparticle vibrational dynamics, as demonstrated by our comparative investigations with other UTEM imaging approaches on the same nanoprisms and under identical optical excitation conditions (27).

To determine the specific vibrational modes excited by laser pulses, we performed a finite-element continuum mechanical simulation based on the actual geometry of Au nanoprism (*Materials and Methods* and *SI Appendix*, Figs. S4 and S5). *SI Appendix*, Fig. S4 *C* and *D* shows two in-plane dilation eigenmodes, M_{d1} and M_{d2}, which are the lowest-frequency vibrational modes previously found in Au nanoprisms on glass substrates through ultrafast optical spectroscopy (17). However, these modes, with the frequencies of 18.6 (M_{d1}) and 22.4 (M_{d2}) GHz, vibrate still faster than any of the ones displayed in our experimental data (Fig. 1*C*). We, therefore, further examined the finite-element analysis data with smaller frequencies. As illustrated in *SI Appendix*, Fig. S5, a total of nine eigenmodes (modes 1 to 9) were found to exist in the frequency range of 0 to 13.5 GHz which encompasses all the frequency peaks in Fig. 1*C* (as indicated with a shaded rectangle). Among them, modes 7 to 9 exhibit marked structural deformation in the nanoprism. As shown in Fig. 2 *C* and *D* (for modes 8 to 9), the deformation occurs mainly at the corners, either by bending upward/downward (m_B) or twisting along a bisector axis closer to graphene surface (m_T). These motions lead to comparatively higher oscillation amplitude at the periphery of nanoparticles (corners and edges). On the contrary, a much lower degree of deformation appears in the first six lower-frequency modes, especially modes 1 to 3, which mainly exhibit a periodical tilting/rotation of the entire nanoprism (Fig. 2 *A* and *B* and *SI Appendix*, Fig. S5). These oscillations occur mainly due to the mechanical deformation of graphene substrates, with the frequencies related to the dimensions of graphene films. It is worth noting that the overall tilting/rotation of Au nanoclusters on graphene substrates subjected to optical excitation has been experimentally observed through ultrafast electron diffractions (31). In UHS-CDF imaging, the tilting motions only lead to an overall change of image intensities within the nanoprisms and do not produce contrast signals in ISD maps.

With reference to the finite-element analysis, we performed a curve fit of the I/I_0-t trace (Fig. 1*B*) by employing a sum of damped harmonic oscillation functions (*Materials and Methods*). The calculated eigenfrequencies (4.3, 7.4, 7.6, 10.2, and 12.5 GHz) that best match the experimental frequency peaks are adopted as invariables for least-squares fitting calculations. As shown in Fig. 1*B*, the fitting curve (dark gray solid line) exhibits reasonable agreement with the experimental I/I_0-t trace (*SI Appendix*, Table S1). This elucidates that the multimode vibrations presented in the graphene-supported Au nanoprism correspond to the bending/torsional motions of the nanoprism, accompanied by an overall tilting effect. Given that most of these

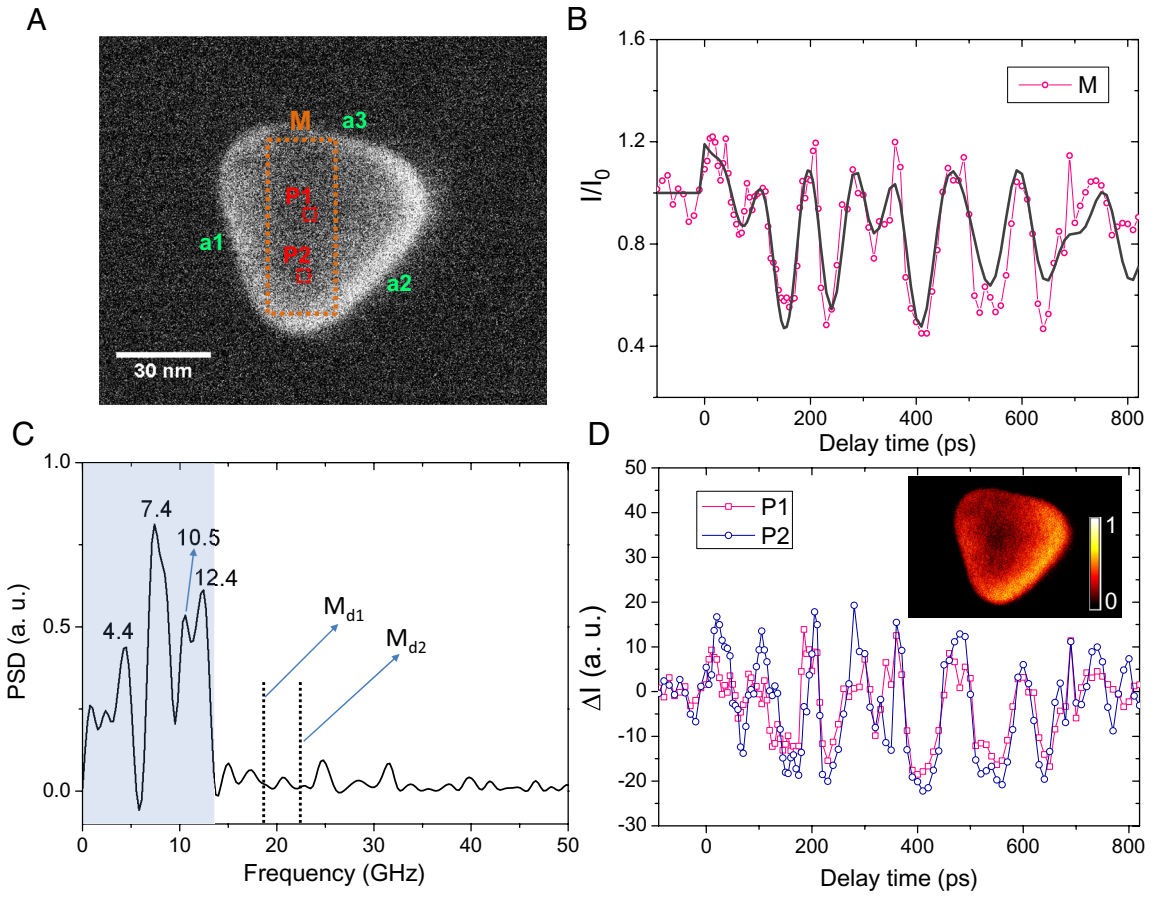

Fig. 1. Structural dynamics of individual Au nanoprisms on graphene substrates. (*A*) A UHS-CDF image (t < 0) recorded for an Au nanoprism with equilateral triangular shape. a1:a2:a3 = 1:0.99:0.98 (a1, a2, and a3 denote the length of sides). (*B*) Temporal changes of relative image intensity (I/I_0) measured from the rectangular region M marked in (*A*). A curve fit is displayed as an overlaying curve (thicker solid line). (*C*) FFT spectrum of the whole trace in (*B*), i.e., all the data points at t ≥ 0. PSD: power spectral density. The dotted lines indicated with M_{d1} and M_{d2} stand for the frequencies of two in-plane dilation eigenmodes determined by finite-element analysis (*SI Appendix*, Fig. S4 *C* and *D*). The presence of two minor peaks at 24.8 and 31.6 GHz is attributed to the measurement uncertainty associated with complicated metal–graphene interactions. (*D*) ΔI–t traces extracted from the square regions P1 and P2 marked in (*A*). The inset shows an intensity SD map generated based on the full image series (t ≥ 0). The color bar displayed in the *Inset* represents normalized intensities.

modes do not have the threefold rotational symmetry as displayed in the dilation modes M_{d1} and M_{d2}, their superimposition should lead to a lower-symmetry, heterogeneous vibration pattern. This is indeed directly mapped in the time-delay image series of the Au nanoprism (Movie S1).

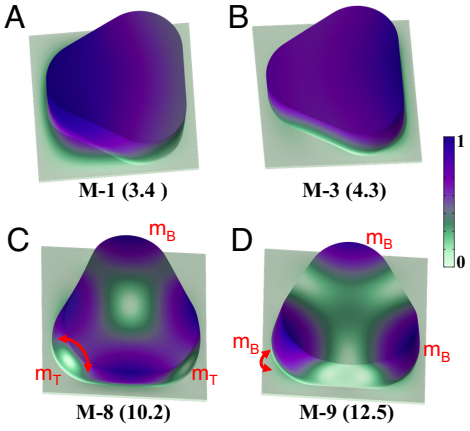

Fig. 2. Finite-element continuum mechanical analysis for the Au nanoprism in Fig. 1*A*. (*A* and *B*) Two selected eigenmodes mainly displaying periodical tilting motion around an edge or a corner of the nanoprism (see *SI Appendix*, Fig. S5 for details). (*C* and *D*) Two selected eigenmodes featuring marked deformation of the nanoprism, in which m_B and m_T denote the bending and torsion motions, respectively. The color bar, common to (*A*–*D*), represents normalized displacements of the nanoprism (with respect to their respective displacement maxima).

Acoustic vibrations in metal nanoparticles are usually launched during the course of electron and lattice thermalization after initial photon absorption and electron excitation (8, 32). For noble metal nanoparticles with an anisotropic shape, strong and nonuniform optical responses occur when there exists a frequency/energy match between their localized surface plasmon resonances (LSPR) and the excitation laser pulses (33, 34). Large-amplitude, intrinsic acoustic vibrations can accordingly be launched under this situation regardless of the possible contribution from supporting substrates. By using monochromatic electron energy loss spectroscopy (EELS) in an aberration-corrected scanning TEM, we performed the surface plasmon measurements for individual Au nanoprisms on graphene substrates without photoexcitation (*Materials and Methods*) (35). As shown in Fig. 3*A*, three LSPR modes are observed, which occur at the corners (L-1), edges (L-2), and center (L-3). The pump pulses used in our UHS-CDF imaging have a photon energy of 2.40 eV, which matches with that of the LSPR modes L-3 (2.33 eV) and L-2 (2.07 eV) but deviates significantly from that of L-1 (1.57 eV) that has the highest resonance amplitude. This suggests the absence of strong intrinsic acoustic vibrations in the nanoprisms. The effect of graphene substrates on vibrational dynamics should thus be considered. In fact, for light-absorbing and conductive materials used as substrates, electron and phonon thermalization processes in metal nanoparticles

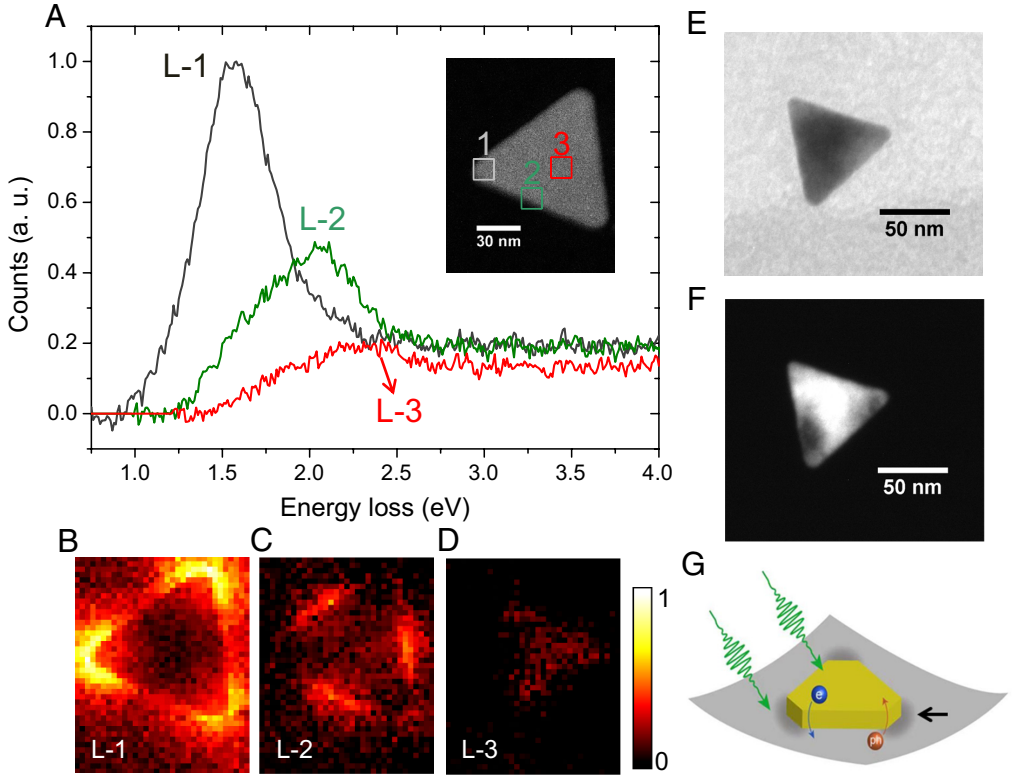

Fig. 3. Formation analysis of the complicated multimode vibrations in graphene-supported Au nanoprisms. (*A–D*) Local surface plasmon resonances investigated by monochromatic EELS at the natural (nonpumped) state. (*A*) Background-subtracted EELS spectra obtained from three typical regions (1 to 3) in the nanoprism as marked in the *Inset*. (*B–D*) EELS maps generated with respect to the three LSPR modes L-1, L-2, and L-3 corresponding to energy losses of 1.57, 2.07, and 2.33 eV, respectively. The color bar (common to all the three modes) denotes EELS signal intensity, which is normalized to the intensity maximum and minimum of the L-1 map. (*E* and *F*) BF and DF-TEM images of an individual nanoprism displaying marked local strain (without photoexcitation). (*G*) Schematic illustration of photoinduced extrinsic electron–phonon interactions across the interface and the presence of internal stresses around the corner regions (indicated with the black arrow).

are always accompanied by metal–substrate interactions, considering the discrepancy in their electron/phonon coupling times. Charge transfer across metal–graphene interfaces has been directly observed by X-ray photoelectron spectroscopy and Raman spectroscopy (36, 37). The structural dynamics of Au nanoclusters on amorphous carbon films investigated by ultrafast electron diffractions demonstrate the existence of extrinsic electron/phonon interactions and heat flow across the interfaces (38). Such extrinsic interactions should also occur in the Au nanoprisms on graphene films. Upon photoexcitation, hot electrons in graphene membranes can efficiently lose energy through the emission of optical phonons within ~200 fs (39), i.e., 1 to 2 orders of magnitude shorter than the electron–phonon coupling time of Au nanoobjects (5 to 15 ps) (23, 40–42). However, the extrinsic electron/phonon interactions cannot be directly bound to the observation of bending/torsional modes, as no evidence shows that they have a clear preference for the excitation of one or more of certain vibrational modes. Future advancements of UTEM instruments may help visualize this reaction process in real space and further enhance our understanding of the mechanism.

Under similar laser excitation and imaging conditions, we also measured the structural dynamics of pure graphene membranes through UHS-CDF imaging (*SI Appendix*, Fig. S6). The data do not exhibit marked acoustic vibrations, suggesting the absence of strong vibrational coupling between Au nanoprisms and graphene film. Nevertheless, suspended graphene membranes are always populated with intrinsic roughness/ripples to maintain long-range order of the 2D crystals (43, 44). More severe structural deformation is expected to emerge when Au nanoprisms are deposited on the free-standing films, as confirmed in our static TEM study of both isolated and aggregated nanoprisms (without photoexcitation). In some of them, especially for those without obvious corner truncation, local deformation is rather prominent and can even be directly mapped through BF or DF TEM imaging (Fig. 3 *E* and *F* and *SI Appendix*, Fig. S7). This is further corroborated by high-resolution TEM imaging and geometric-phase analysis (*SI Appendix*, *Notes* and Fig. S8). These observations illustrate that a certain degree of lattice stresses already appears at the Au–graphene contact regions (typically around the nanoprism corners) even in the natural state. The nanoprisms on graphene supports, therefore, exhibit significantly different mechanical states from those nanoparticles in liquids or on bulk substrates do (1, 12, 17). In the latter case, dilation modes are readily launched because the resulting displacement fields match more closely with the lattice expansion dynamics induced by homogeneous laser heating. The conformity state is, however, altered in Au nanoprisms on graphene films because of the appearance of contact stresses and concomitant lattice anharmonicity at the corner regions. The preexisting deformation potential regulates and directs the relaxation process of photoexcited nanoparticles, which, perhaps with the aid of Au–graphene electron/phonon interactions as mentioned above, finally leads to the formation of bending/torsional modes. The possibility of generating sufficient contact stress to initiate the bending/torsional motions should be pertinent to both nanoparticle shapes and supporting substrates. For those nanoparticles without the inclusion of corners/tips, such as nanospheres and nanorods, these motions may not be launched even with the use of graphene substrates (9). We also identified that their excitation

is not associated with the presence of capping agents. As shown in *SI Appendix*, Fig. S9, low-frequency vibrational modes still dominate in the relaxation process of Au nanoprisms even with the capping agents removed. In addition, our extensive experiments and analysis show that the number of low-frequency bending/torsional modes does not remain constant between different nanoparticles, as reflected in Fig. 1*C* and *SI Appendix*, Fig. S9 *B* and *D*. This could be mainly attributed to the complexity and nonuniformity of Au–graphene interfacial status (*SI Appendix*, Fig. S6*A*), which leads to the variation of contact stresses between different nanoparticles. A schematic representation of the graphene-assisted relaxation dynamics of Au nanoprisms is displayed in Fig. 3*G*.

Meanwhile, we have also noticed that Au nanoprisms with nonequilateral triangular shapes exhibit even more marked heterogeneous oscillation patterns. Fig. 4 shows UHS-CDF imaging investigations of an irregularly shaped Au nanoprism (a1:a2:a3=1:1.14:0.88) on graphene substrates (Fig. 4*A*). Direct analysis of image contrast from the time-delay data series (Fig. 4*C* and Movie S2) reveals the occurrence of bending or twisting motions at the corners at the early relaxation stage TS-1 (0 to 190 ps, as indicated in Fig. 4 *B*, *Bottom*), similar to equilateral triangular–shaped nanoprisms. Intrananoparticle intensity measurements (Fig. 4*B*) display almost zero oscillation amplitude at the center region P4, which leads to the formation of a dark core in the ISD map generated for TS-1 (Fig. 4 *A*, *Inset*). Dissimilar vibrational behaviors, however, were observed during the ensuing relaxation stage TS-2. As shown in Fig. 4*C* (and *SI Appendix*, Fig. S10 for more details), the nanoprism exhibits significantly more marked twisting motions involving the entire Au nanoprism along a bisector through the immobile corner C_1 (which replaces the center as a new anchoring site). The transition of anchoring sites is also reflected in the ΔI–t measurements, which illustrate the shift

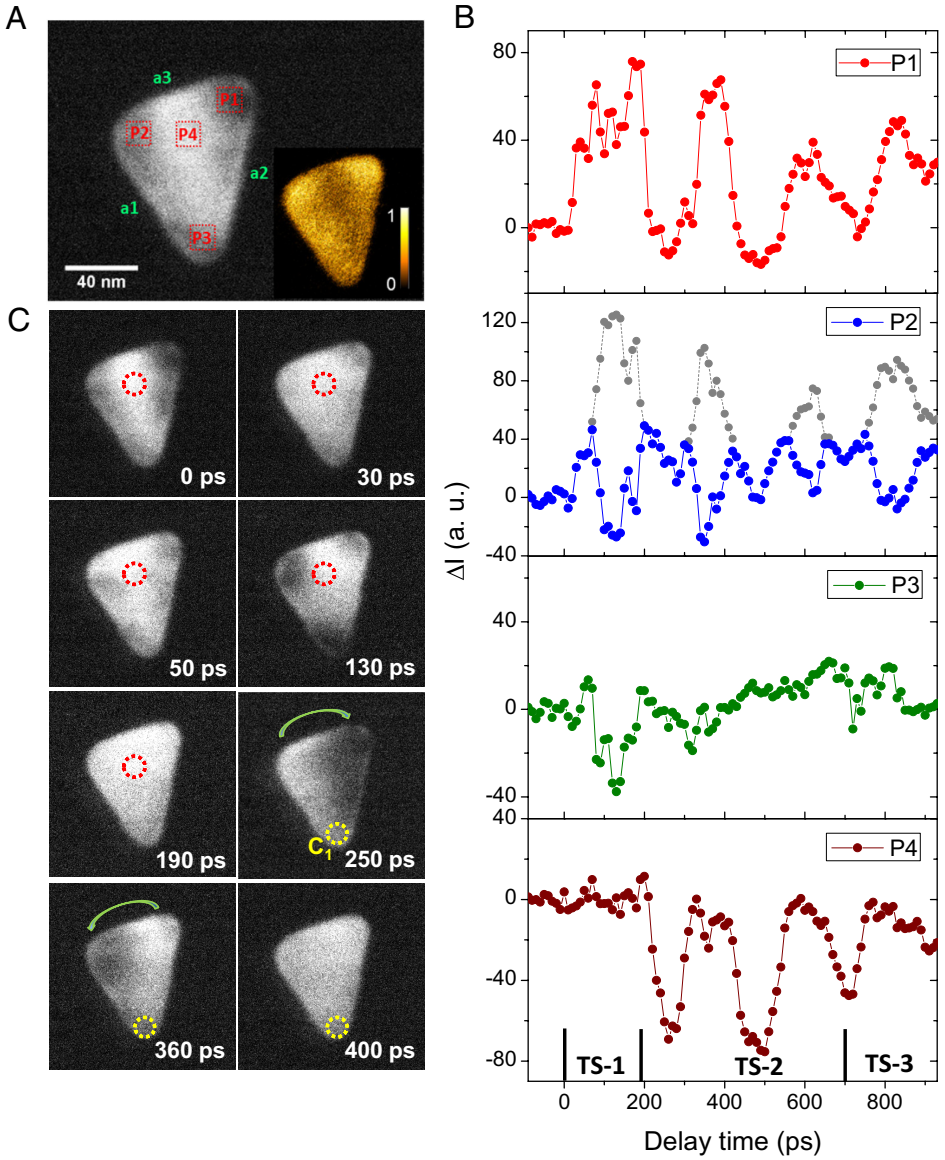

Fig. 4. Structural dynamics of Au nanoprisms with an irregular triangular shape. (*A*) An individual frame (t < 0) from a time-delay image series. a1:a2:a3=1:1.14:0.88 (a1, a2, and a3 denote the length of sides). The *Inset* shows the intensity SD map generated for the early relaxation stage TS-1 (0 to 190 ps) as marked at the bottom of (*B*). (*B*) ΔI–t traces measured from the square regions P1-P4 marked in (*A*). The gray line displayed in P2 denotes the actual vibration response regained with the exclusion of peak bifurcation. (*C*) Selected frames showing the bending/torsional motions arising at the corners initially (0 to 190 ps), followed by overall twisting motions of the whole nanoprism. The red and yellow circles indicate anchoring points. C1 indicates the bottom corner of the nanoprism.

of the approximate zero-amplitude oscillation regions from P4 at TS-1 to P3 at TS-2 (Fig. 4*B*). The observation of the overall twisting behaviors may be associated with the breaking of threefold rotational symmetry in irregularly shaped nanoprisms. The fact that the longest bisector serves as a twist axis indicates that such motions are more preferably launched along this direction. Compared with localized bending/torsional motions, the overall twisting mode appears to involve more rapid energy decay. As illustrated in Fig. 4*B*, the reappearance of (smaller) intensity peaks in P3 at TS-3 suggests a restoration of local bending/torsional motions when the preceding overall twisting movements become significantly damped and thus less dominant. These heterogeneous dynamics behaviors are also largely reflected in the temporal measurements of the lateral dimensions of Au nanoprisms (*SI Appendix*, Fig. S11), although detailed information about intrananoparticle vibrational evolution cannot be obtained via the analysis approach.

In conclusion, we have demonstrated the launch of bending and torsional modes and their rich relaxation dynamics in individual Au nanoprisms induced by photoexcitation. The preferential excitation of these modes is associated with special mechanical contact states between Au nanoparticles and free-standing graphene membranes. The shape effect on vibrational evolution was also investigated, which revealed a mode transition from localized bending/twisting to overall twisting motions in irregularly shaped Au nanoprisms. Our study highlights that, by optimizing sample designs and using high spatiotemporal resolution imaging approaches, detailed information on relaxation dynamics can be extracted even in the presence of complicated optical responses. The method demonstrated here can be easily extended to the observation of other nanoparticles with various sizes and morphologies on different supporting substrates at the subnanoparticle level. A thorough investigation of optical responses and structural dynamics performed in this manner should help to better understand the fundamental properties and functionalities of nanostructured materials and facilitate their applications.

Materials and Methods

TEM Specimen Preparation and Characterization. The chemically synthetic Au nanoprisms (Zhongkeleiming, Inc.) are capped with hexadecyl trimethyl ammonium bromide (CTAB). The sample solution was diluted in deionized water and then purified via centrifugation (~7,100 × g/10 min). To prepare TEM samples, a small drop of nanoparticle solution was drop-casted onto 2,000-mesh Cu grids covered with graphene films (Graphene Laboratories Inc.). The synthetic Au nanoprisms mostly exhibit approximately equilateral triangular shapes, with a corner-truncated side length of 70 nm and a thickness of 20 nm on average. They are located on the substrates with the orientation along <111> zone axis and typically surrounded by {-422} side facets (*SI Appendix*, Fig. S1).

UTEM Experiments. Our ultrafast TEM experiments were performed with a 200-kV FEI (Field Electron and Ion) Tecnai G20 ultrafast electron microscope coupled with a Clark IMPULSE laser (pulse width: 210 fs; center wavelength: 1,035 nm) (42). Frequency-quadrupled and -doubled laser pulses were introduced into the TEM column to excite LaB_6 photocathodes and the specimen, respectively. UHS-CDF imaging was typically performed on Au nanoprisms on few-layer graphene films by employing a mildly converged electron beam of ~2 mrad, an objective aperture of 4 mrad, and a pulse repetition rate of 200 kHz. To operate approximately at single-electron imaging conditions, the probe power was set to generate about 55 electrons per timed packet, which enables an effective exclusion of the Coulomb repulsion effect. Structural dynamics of Au nanoprisms were initiated using pump laser beams with a spot diameter of ~67 μm and excitation fluences of 2.8 to 4.2 mJ/cm^2.

UTEM Data Processing and Analysis. UHS-CDF image series were first aligned using crosscorrelation functions. This was conducted for all the recorded frames, except for the first several ones that were acquired immediately after sample tilting and beam alignment when the system had not yet reached a steady state. Based on the aligned image sequences, the intensities were measured by integrating over the imaging area of the whole or a part of a nanoparticle, followed by the subtraction of background intensities determined based on a ring region (with the identical area by normalization) around the nanoparticle for each frame. The vibrational frequency information was obtained by performing FFT analysis over the whole traces of intensity data, i.e., all the data points excluding those with negative delay times. The FFT results were plotted with spline curves.

A total of N damped harmonic oscillation functions, as shown in function [**1**], were used for fitting the UTEM intensity data.

$$I(t) = \sum_{i=1}^{N} A_i \cos\left[\frac{2\pi}{T_i}\left(t + t0_i\right)\right] e^{-\frac{t}{td_i}} + I0_i. \qquad [\mathbf{1}]$$

Here, A_i, T_i, $t0_i$, td_i, and $I0_i$ denote the oscillation amplitude, period, initial time, decay time, and intensity offset of the ith damping oscillation mode, respectively. The fitting was performed for the whole intensity I/I_0 trace (0 to 820 ps) in Fig. 1*B* with the calculated eigenfrequencies best matching the experimental frequency peaks assigned to T_i. Note that the two eigenmodes with similar frequencies (7.4, 7.6 GHz) are used to match the experimental one (7.4 GHz) that features the highest PSD. The resulting data are shown in *SI Appendix*, Table S1 and plotted in Fig. 1*B* as an overlaying curve (the curve is also extended to negative time-delay points by simply setting their values to one).

Temporal dimensional changes of Au nanoprisms were determined by measuring the difference in position coordinates (x, in subpixels) of a corner and its opposite edge through intensity fitting with the logistic sigmoid function [**2**].

$$I = I_{NP} + \frac{I_S - I_{NP}}{1 + e^{\frac{x - x_0}{w}}}. \qquad [\mathbf{2}]$$

Here, I_S, I_{NP}, x_0, and w denote the intensities at substrates and nanoprisms, the position coordinate of nanoprism corners/edges, and the width of logistic growth, respectively.

Monochromatic EELS. To determine the LSPR of Au nanoprisms, EELS experiments were conducted on an FEI double-aberration-corrected Titan3 G2 S/TEM instrument incorporated with a monochromator. An accelerated voltage of 60 kV was adopted to decrease the radiation damage of the corrected electron probe to graphene membranes. EELS spectrum images of Au nanoparticles were acquired with a convergence angle of 24 mrad, a collection angle of 18.9 mrad, and a dispersion of 0.01 eV per channel. A constant energy width of 0.1 eV (which is also the instrument energy resolution) was used for extracting all the EELS maps corresponding to various LSPR modes.

Finite-Element Continuum Mechanical Simulation. The calculations were conducted using COMSOL Multiphysics software (Solid Mechanics module). Au nanoprisms were modeled by considering their actual geometries. For the nanoprism in Fig. 1*A*, a regular triangular prism was generated with a side length of 96 nm (truncated with a fillet radius of 19 nm) and a thickness of 20 nm. It is surrounded by a layer of capping agents (PMMA, 2 nm) (ref. 8) and lies on a graphene membrane (80 × 80 × 2 nm), as shown in *SI Appendix*, Fig. S4 *A* and *B*. The four side faces of the graphene membrane are set as fixed constraints for calculations. The Young's modulus/Poisson ratio used for Au, PMMA, and graphene is 64 GPa/0.42 (ref. 9), 3.2 Gpa/0.38 (ref. 45), and 2.0 Tpa/0.16 (ref. 9), respectively.

Data, Materials, and Software Availability. All study data are included in the article and/or supporting information.

ACKNOWLEDGMENTS. We thank Xiaofang Kang for her help in the UTEM and EELS experiments. This research was supported by the National Natural Science Foundation of China (Grant No. 51571035).

Author affiliations: [a]Beijing Institute of Nanoenergy and Nanosystems, Chinese Academy of Sciences, Beijing 100083, China; [b]School of Nanoscience and Technology, University of Chinese Academy of Sciences, Beijing 100049, China; [c]National Laboratory of Solid State Microstructures, Jiangsu Key Laboratory of Artificial Functional Materials, College of Engineering and Applied Sciences and Collaborative Innovation Center of Advanced Microstructures, Nanjing University, Nanjing 210093, China; [d]Department of Physics, University of Warwick, Coventry CV4 7AL, UK; [e]The Institute for Technological Sciences, Wuhan University, Wuhan 430072, China; [f]School of Materials Science and Engineering, Georgia Institute of Technology, Atlanta, GA 30332-0245; [g]State Key Laboratory for Mesoscopic Physics and Frontiers Science Center for Nano-Optoelectronics, School of Physics, Peking University, Beijing 100871, China; and [h]Center on Nanoenergy Research, School of Physical Science and Technology, Guangxi University, Nanning 530004, China

1. A. Crut, P. Maioli, N. Del Fatti, F. Vallee, Acoustic vibrations of metal nano-objects: Time-domain investigations. *Phys. Rep.* **549**, 1–43 (2015).
2. D. Bozyigit *et al.*, Soft surfaces of nanomaterials enable strong phonon interactions. *Nature* **531**, 618–622 (2016).
3. J. C. Levy, A phonon-assisted process in catalytic phenomena. *Jpn. J. Appl. Phys.* **13**, 465–468 (1974).
4. T. Takagahara, Electron–phonon interactions in semiconductor nanocrystals. *J. Lumin.* **70**, 129–143 (1996).
5. D. G. Cahill *et al.*, Nanoscale thermal transport. II. 2003–2012. *Appl. Phys. Rev.* **1**, 011305 (2014).
6. G. V. Hartland, Optical studies of dynamics in noble metal nanostructures. *Chem. Rev.* **111**, 3858–3887 (2011).
7. J. N. Clark *et al.*, Ultrafast three-dimensional imaging of lattice dynamics in individual gold nanocrystals. *Science* **341**, 56–59 (2013).
8. D. T. Valley, V. E. Ferry, D. J. Flannigan, Imaging intra- and interparticle acousto-plasmonic vibrational dynamics with ultrafast electron microscopy. *Nano Lett.* **16**, 7302–7308 (2016).
9. Y.-J. Kim, H. Jung, S. W. Han, O.-H. Kwon, Ultrafast electron microscopy visualizes acoustic vibrations of plasmonic nanorods at the interfaces. *Matter* **1**, 481–495 (2019).
10. M. Hu *et al.*, Vibrational response of nanorods to ultrafast laser induced heating: Theoretical and experimental analysis. *J. Am. Chem. Soc.* **125**, 14925–14933 (2003).
11. W. Y. Huang, W. Qian, M. A. El-Sayed, Coherent vibrational oscillation in gold prismatic monolayer periodic nanoparticle arrays. *Nano Lett.* **4**, 1741–1747 (2004).
12. L. Bonacina, A. Callegari, C. Bonati, F. van Mourik, M. Chergui, Time-resolved photodynamics of triangular-shaped silver nanoplates. *Nano Lett.* **6**, 7–10 (2006).
13. Y. Tang, M. Ouyang, Tailoring properties and functionalities of metal nanoparticles through crystallinity engineering. *Nat. Mater.* **6**, 754–759 (2007).
14. N. Del Fatti *et al.*, Coherent acoustic mode oscillation and damping in silver nanoparticles. *J. Chem. Phys.* **110**, 11484–11487 (1999).
15. M. Pelton *et al.*, Damping of acoustic vibrations in gold nanoparticles. *Nat. Nanotechnol.* **4**, 492–495 (2009).
16. M. A. van Dijk, M. Lippitz, M. Orrit, Detection of acoustic oscillations of single gold nanospheres by time-resolved interferometry. *Phys. Rev. Lett.* **95**, 267406 (2005).
17. J. Burgin *et al.*, Time-resolved investigation of the acoustic vibration of a single gold nanoprism pair. *J. Phys. Chem. C* **112**, 11231–11235 (2008).
18. G. Beane, T. Devkota, B. S. Brown, G. V. Hartland, Ultrafast measurements of the dynamics of single nanostructures: A review. *Rep. Prog. Phys.* **82**, 016401 (2019).
19. N. Del Fatti, C. Voisin, D. Christofilos, F. Vallée, C. Flytzanis, Acoustic vibration of metal films and nanoparticles. *J. Phys. Chem. A* **104**, 4321–4326 (2000).
20. B. Ostovar *et al.*, Acoustic vibrations of Al nanocrystals: Size, shape, and crystallinity revealed by single-particle transient extinction spectroscopy. *J. Phys. Chem. A* **124**, 3924–3934 (2020).
21. D. Laage, T. Elsaesser, J. T. Hynes, Water dynamics in the hydration shells of biomolecules. *Chem. Rev.* **117**, 10694–10725 (2017).
22. J. Briand *et al.*, Coherent ultrafast torsional motion and isomerization of a biomimetic dipolar photoswitch. *Phys. Chem. Chem. Phys.* **12**, 3178–3187 (2010).
23. B. Barwick, H. S. Park, O.-H. Kwon, J. S. Baskin, A. H. Zewail, 4D imaging of transient structures and morphologies in ultrafast electron microscopy. *Science* **322**, 1227–1231 (2008).
24. H. S. Park, J. S. Baskin, B. Barwick, O.-H. Kwon, A. H. Zewail, 4D ultrafast electron microscopy: Imaging of atomic motions, acoustic resonances, and moire fringe dynamics. *Ultramicroscopy* **110**, 7–19 (2009).
25. T. Danz, T. Domröse, C. Ropers, Ultrafast nanoimaging of the order parameter in a structural phase transition. *Science* **371**, 371–374 (2021).
26. L. Reimer, H. Kohl, *Transmission Electron Microscopy Physics of Image Formation* (Springer, Berlin, ed. 5, 2008).
27. L. Tong, J. Yuan, Z. W. Zhang, J. Tang, Z. W. Wang, Nanoscale subparticle imaging of vibrational dynamics using dark-field ultrafast transmission electron microscopy. *Nat. Nanotechnol.* **18**, 145–152 (2023).
28. C. Xu, X. Wang, J. Zhu, Graphene–Metal particle nanocomposites. *J. Phys. Chem. C* **112**, 19841–19845 (2008).
29. P. Wang, O. Liang, W. Zhang, T. Schroeder, Y.-H. Xie, Ultra-sensitive graphene-plasmonic hybrid platform for label-free detection. *Adv. Mater.* **25**, 4918–4924 (2013).
30. B. Seger, P. V. Kamat, Electrocatalytically active graphene-platinum nanocomposites. Role of 2-D carbon support in PEM fuel cells. *J. Phys. Chem. C* **113**, 7990–7995 (2009).
31. T. Vasileiadis *et al.*, Ultrafast rotational motions of supported nanoclusters probed by electron diffraction. *Nanoscale Horiz.* **4**, 1164–1173 (2019).
32. S. I. Anisimov, B. L. Kapeliovich, T. L. Perelman, Electron emission from metal surfaces exposed to ultrashort laser pulses. *J. Exp. Theor. Phys.* **66**, 375–377 (1974).
33. V. Amendola, R. Pilot, M. Frasconi, O. M. Maragò, M. A. Iatì, Surface plasmon resonance in gold nanoparticles: A review. *J. Phys. Condens. Matter* **29**, 203002 (2017).
34. A. K. Pearce, T. R. Wilks, M. C. Arno, R. K. O'Reilly, Synthesis and applications of anisotropic nanoparticles with precisely defined dimensions. *Nat. Rev. Chem.* **5**, 21–45 (2021).
35. Y. Zeng, S. J. Madsen, A. B. Yankovich, E. Olsson, R. Sinclair, Comparative electron and photon excitation of localized surface plasmon resonance in lithographic gold arrays for enhanced Raman scattering. *Nanoscale* **12**, 23768–23779 (2020).
36. J. Lee, K. S. Novoselov, H. S. Shin, Interaction between metal and graphene: Dependence on the layer number of graphene. *ACS Nano* **5**, 608–612 (2011).
37. Y. Du *et al.*, Enhanced light-matter interaction of graphene-gold nanoparticle hybrid films for high-performance SERS detection. *J. Mater. Chem C* **2**, 4683–4691 (2014).
38. T. Vasileiadis *et al.*, Ultrafast heat flow in heterostructures of Au nanoclusters on thin films: Atomic disorder induced by hot electrons. *ACS Nano* **12**, 7710–7720 (2018).
39. S. Ulstrup *et al.*, Ultrafast electron dynamics in epitaxial graphene investigated with time- and angle-resolved photoemission spectroscopy. *J. Phys. Condens. Matter.* **27**, 164206 (2015).
40. J. Hohlfeld *et al.*, Electron and lattice dynamics following optical excitation of metals. *Chem. Phys.* **251**, 237–258 (2000).
41. S. Schäfer, W. Liang, A. H. Zewail, Structural dynamics of nanoscale gold by ultrafast electron crystallography. *Chem. Phys. Lett.* **515**, 278–282 (2011).
42. D. S. Li, Z. L. Wang, Z. W. Wang, Revealing electron-phonon interactions and lattice dynamics in nanocrystal films by combining in situ thermal heating and femtosecond laser excitations in 4D transmission electron microscopy. *J. Phys. Chem. Lett.* **9**, 6795–6800 (2018).
43. J. C. Meyer *et al.*, The structure of suspended graphene sheets. *Nature* **446**, 60–63 (2007).
44. A. Fasolino, J. H. Los, M. I. Katsnelson, Intrinsic ripples in graphene. *Nat. Mater.* **6**, 858–861 (2007).
45. K. Yan *et al.*, The influence of elastic strain on catalytic activity in the hydrogen evolution reaction. *Angew. Chem. Int. Ed. Engl.* **55**, 6175–6181 (2016).